# Retrieval of humidity and temperature profiles over the oceans from INSAT 3D satellite radiances

C Krishnamoorthy, Deo Kumar and C Balaji*

*Indian Institute of Technology Madras, Chennai 600 036, India.*
**Corresponding author. e-mail: balaji@iitm.ac.in*

In this study, retrieval of temperature and humidity profiles of atmosphere from INSAT 3D-observed radiances has been accomplished. As the first step, a fast forward radiative transfer model using an Artificial neural network has been developed and it was proven to be highly effective, giving a correlation coefficient of 0.97. In order to develop this, a diverse set of physics-based clear sky profiles of pressure ($P$), temperature ($T$) and specific humidity ($q$) has been developed. The developed database was further used for geophysical retrieval experiments in two different frameworks, namely, an ANN and Bayesian estimation. The neural network retrievals were performed for three different cases, viz., temperature only retrieval, humidity only retrieval and combined retrieval. The temperature/humidity only ANN retrievals were found superior to combined retrieval using an ANN. Furthermore, Bayesian estimation showed superior results when compared with the combined ANN retrievals.

## 1. Introduction

Remote sensing of the atmosphere and ocean has gained considerable impetus in view of its usefulness in achieving better forecast skill through radiance assimilation. Several data assimilation techniques in both deterministic and stochastic frameworks have been developed in the last few decades. In order to achieve better forecast skill, accurate retrieval of atmospheric parameters are inevitable. Modern developments in satellite meteorology have paved way to accomplish the former. Geostationary satellites whose field of view is fixed over a particular region have proved to have a greater impact on the assimilation. There is a class of deterministic approaches available for the inversion/retrieval of atmospheric profiles from the satellite-observed radiances. Hewison (2007) demonstrated the use of 1D-VAR retieval technique to retrieve both temperature and humidity profiles from a ground-based microwave radiometer. This showed a considerable improvement in the retrievals. Similarly, Marécal and Mahfouf (2000) used the variational approach for simultaneous retrieval of temperature and humidity from TRMM precipitation radar. They also studied the impact of the observation error in the retrieval and they were subsequently assimilated in the ECMWF 4d-VAR system. Phalippou (1996) proposed a new variational retrieval method based on the nonlinear optimal estimation theory for retrieving humidity profiles from SSM/I radiances. The capability of neural networks was employed by Jones *et al.* (1999) to derive monthly averages of the surface specific humidity and air temperature. Churnside *et al.* (1994) also used neural networks for inversion of microwave radiometer data to obtain temperature profiles. Shi (2001) demonstrated the usage of feed-forward back propagation neural network for temperature retrieval from AMSU-A measurements. Jieying *et al.* (2010) proposed an algorithm based on neural networks with morilet

**Keywords.** Artificial neural networks; INSAT 3D; humidity; temperature; maximum likelihood; Bayesian.

and mexihat function. They demonstrated the humidity retrieval performance from FENGYUN-3A datasets. Passive microwave humidity retrievals using a multi-layered feed-forward neural network was attempted by Cabrera-Mercader and Staelin (1994). They demonstrated the superiority of neural network retrievals over statistical and other physical retrieval schemes. Ajil *et al.* (2010) proposed a neuro-fuzzy logic scheme for retrieving temperature and humidity from GOES-12 sounder channels.

Improvements in Bayesian statistics have also inspired many researchers and the power of invoking prior knowledge in the retrieval framework has improved the retrieval performance significantly. Marzano *et al.* (2010) presented an iterative Bayesian retrieval algorithm for dual-polarized radars. McFarlane *et al.* (2002) presented a new algorithm for optical depth and liquid water content retrieval from millimeter wavelength radar reflectivity. They used the prior distributions calculated from *in-situ* measurements of droplet size distributions. Thapliyal *et al.* (2014) studied the impact of hybrid-regression technique on humidity profile retrieval using an infrared sounder data. Krishnan *et al.* (2012) developed a fast forward model for simulating infrared radiances and demonstrated its far-reaching impact in reducing the computation time required by the traditional line-by-line (LBL) solvers. Ramanujam *et al.* (2011) developed a new PCA-ANN retrieval approach for retrieving the hydrometeor profiles in a raining atmosphere. Bayesian retrievals were also attempted by Balaji and Ramanujam (2013) for retrieving the vertical rainfall structure from MADRAS instrument aboard Megha-Tropiques. In view of the above in this study, a simultaneous retrieval of humidity and temperature has been attempted in two different frameworks namely an artificial neural network and Bayesian estimation. The key highlights of this work are: (1) use of physics-based retrievals and (2) use of actual satellite-observed radiances for the retrievals.

## 2. INSAT 3D

The INSAT 3D satellite launched on 26th July 2013 by ISRO, is one of India's major meteorological satellites. The objectives of the mission are:

- to continuously monitor the oceanic and land surface regions with a multi-channel sounder and imager which are of meteorological importance,
- to provide a quantitative estimate of the temperature and humidity, and
- for satellite aided search and rescue services.

The payload is an advanced very high resolution infrared imager and a 19-channel sounder. The sounder has 18 channels spanning in the infrared region from 3.74 to 14.71 μm and one channel in the visible region of the spectrum with a ground resolution of 10×10 km at nadir for all channels. Table 1 gives the specifications of the infrared sounder payload. There are three modes of operation available in INSAT 3D, viz., full frame mode, programmed normal scan mode and programmed sector scan mode. The different scanning sectors associated with INSAT 3D are shown in figure 1.

The various channels present in INSAT 3D sounder and their respective central wavelengths are shown in table 2. The INSAT 3D measured counts were converted to brightness temperatures (BTs) using the look up tables provided with the Level 1 data. For a fuller discussion on different modes of operation and corrections done on INSAT 3D products, please refer to INSAT 3D catalogue (Katti *et al.* 2006).

## 3. Spectral response functions of INSAT 3D

The spectral response of the instrument channels in the infrared region of the spectrum is shown in figure 2. The spectral response function is convolved with each channel radiance in the following way:

$$\int_0^\infty F(\nu)B(\nu,T_e)d\nu = \int_0^\infty F(\nu)R(\nu)d\nu. \quad (1)$$

Table 1. *Infrared sounder payload specifications.*

| Spectral channels | Spectral range (μm) | Resolution (km) |
|---|---|---|
| Visible | 0.67–0.72 | 10 |
| SWIR (6 channels) | 3.67–4.59 | 10 |
| MWIR (5 channels) | 6.38–11.33 | 10 |
| LWIR (7 channels) | 11.66–14.85 | 10 |

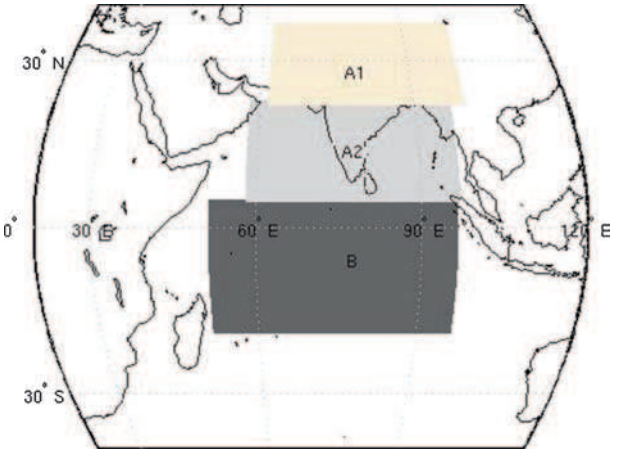


Figure 1. INSAT 3D scanning geometry.

Table 2. *INSAT 3D channel specifications.*

| Channel | Central wavelength (μm) | Bandwidth (μm) | Principal absorbing constituent |
|---|---|---|---|
| 1 | 14.71 | 0.281 | $CO_2$ band |
| 2 | 14.37 | 0.268 | $CO_2$ band |
| 3 | 14.06 | 0.256 | $CO_2$ band |
| 4 | 13.96 | 0.298 | $CO_2$ band |
| 5 | 13.37 | 0.286 | $CO_2$ band |
| 6 | 12.66 | 0.481 | Water vapour |
| 7 | 12.02 | 0.723 | Water vapour |
| 8 | 11.03 | 0.608 | Window |
| 9 | 9.71 | 0.235 | Ozone |
| 10 | 7.43 | 0.304 | Water vapour |
| 11 | 7.02 | 0.394 | Water vapour |
| 12 | 6.51 | 0.255 | Water vapour |
| 13 | 4.57 | 0.048 | $N_2O$ |
| 14 | 4.52 | 0.047 | $N_2O$ |
| 15 | 4.45 | 0.045 | $CO_2$ |
| 16 | 4.13 | 0.0683 | $CO_2$ |
| 17 | 3.98 | 0.0683 | Window |
| 18 | 3.74 | 0.140 | Window |

In equation (1), $\nu$ is the wave number, $F$ is the response of the instrument and $B$ is the Planck's blackbody intensity at $\nu$ and at temperature $T_e$. Finally, $R$ is the intensity measured by the instrument. With this, the convolved radiance can be written as:

$$B = \frac{\sum F(\nu)R(\nu)}{\sum F(\nu)}. \tag{2}$$

## 4. Forward model

The intensity of electromagnetic radiation emerging from top of atmosphere in the infrared region of the spectrum can be given by the radiative transfer equation (RTE).

$$\mu \frac{dI_\eta}{d\tau} = -\kappa_\eta I_\eta + \varepsilon_\eta I_{b\eta}. \tag{3}$$

In equation (3), $I$ is the intensity of the diffuse radiation, $\kappa$ is the absorptivity, $\varepsilon$ is the emissivity and $\tau$ is the optical depth. In the above equation, the scattering effects were neglected due to clear sky conditions. It can be seen that the intensity change within a given optical depth is the sum of attenuation inherent in the medium and augmentation due to emission. Finally, $I_{b\eta}$ is the Planck's blackbody spectral intensity which is a function of wavenumber $\eta$ and temperature ($T$) which can be given as:

$$I_{b\eta} = \frac{c_1 \eta^5}{\exp(c_2 \eta / T) - 1} \tag{4}$$

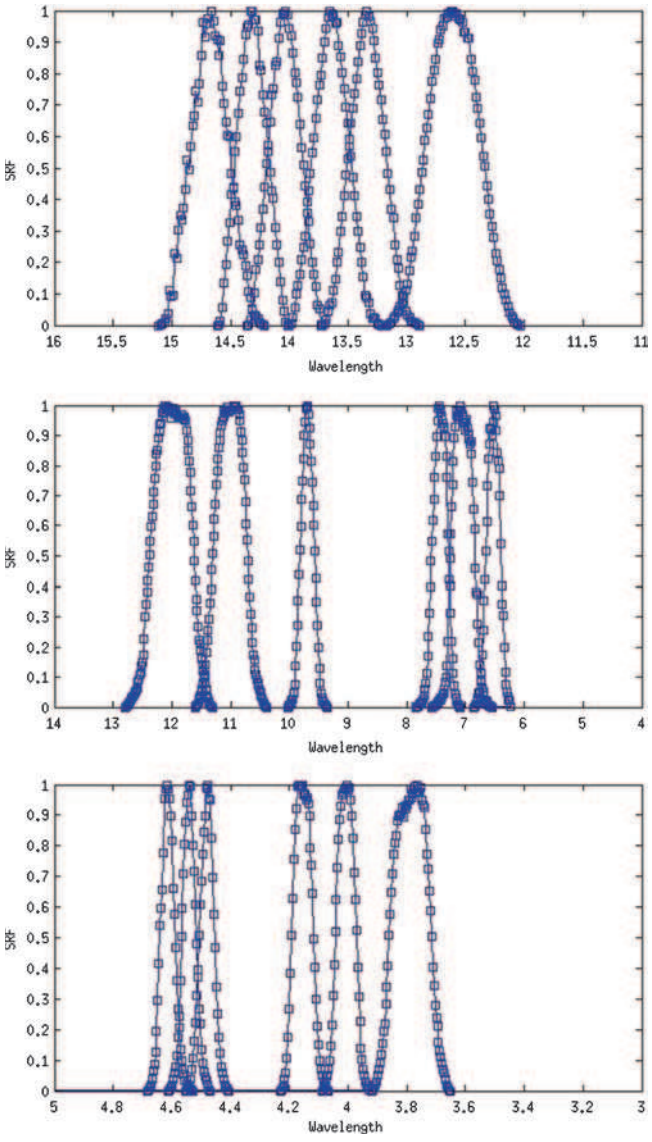


Figure 2. Spectral response function for INSAT 3D channels.

where $c_1$ and $c_2$ are first and second radiation constants respectively. By invoking Kirchoff's law, we can rewrite equation (3) as:

$$\mu \frac{dI_\eta}{d\tau} = -\kappa_\eta I_\eta + \kappa_\eta \frac{c_1 \eta^5}{\exp(c_2 \eta / T) - 1}. \tag{5}$$

In the present study, to simulate accurately the upwelling radiances in the infrared regime of the spectrum, an LBL radiative transfer equation solver is inevitable. LibRadTran (Mayer and Kylling 2005), a community RTE solver for thermal and solar radiation is used. The LBL calculations were carried out with the information on radiative properties from HITRAN (Rothman *et al.* 2005) database. The agreement between the simulated and observed BTs can be seen from the accompanying parity plot (figure 3), which shows a correlation coefficient of 0.98.

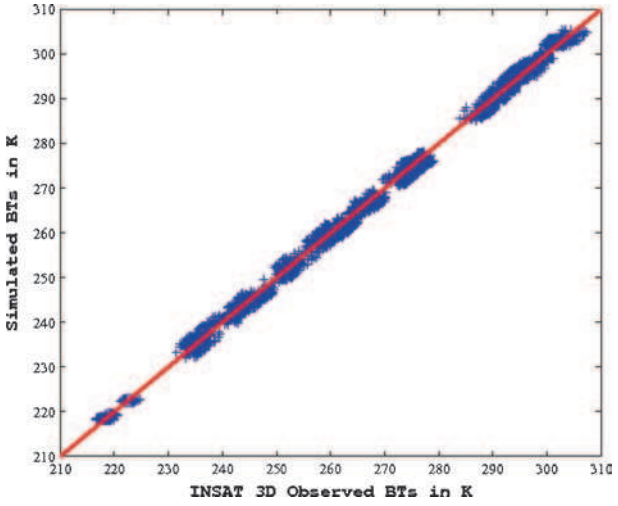


Figure 3. Parity between forward model simulated and observed INSAT 3D BTs.

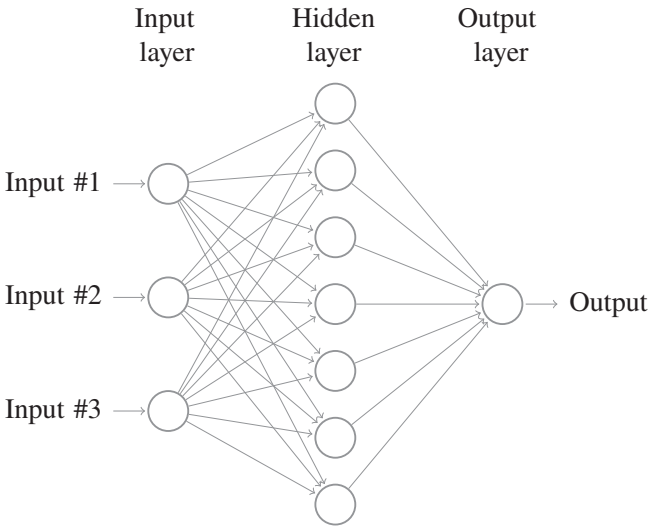


Figure 4. A typical neural network architecture.

## 5. Artificial neural networks

Artificial neural networks (ANN) are considered as a more promising tool for problem involving huge datasets especially when the relationship ceases to be linear. The multi-layer feed-forward back propagation network involves an input layer, a hidden layer and an output layer. There are as many number of neurons as input in the input layer. All the neurons in the hidden layer and input layer are combined with associated weight to form the target output. The optimal weights can be arrived using any of the gradient minimization algorithms. The neurons being building blocks of these neural network architecture can be varied and different transfer functions can be used. One such transfer function that has been widely used is the tan-sigmoidal function which is given as:

$$f = \frac{e^x - e^{-x}}{e^x + e^{-x}}. \tag{6}$$

The output from each of the hidden neuron is calculated as:

$$y_j = f\left(\sum_{i=1}^{n} w_{ij} x_i\right) \tag{7}$$

where $f$ is the transfer function and $w_{ij}$ is the random weights given to each $i$ and $j$th neuron. Finally, the output from the output layer is calculated by adding a linear activation function of the form,

$$o_j = \sum_{i=1}^{n} w_{ij} x_j. \tag{8}$$

During the training of ANN, a minimization technique is used to arrive at the best estimate of the weights $w_{ij}$ for a given set of input and output vector. Once the best network is achieved, the weights are saved and they are tested for accessing the performance.

## 6. ANN-based forward model

In view of the time consuming forward model calculations, a fast forward model is required so as to accelerate the process of retrieval if direct ANN retrievals are not desired and instead ANN is used to drive a more robust retrieval algorithm. Furthermore, each retrieval step may require many forward calculations. The promising performance and the learning capabilities of the ANNs have aspired many researchers for developing an ANN-based fast-forward model. So in this work, a fast forward model has been constructed in the parlance of neural networks. A general architecture of the ANN discussed above is shown in figure 4. The inputs for the ANN are layerwise values of pressure ($P$), temperature ($T$) and specific humidity ($q$) and the outputs are 18 channel BTs corresponding to INSAT 3D.

### 6.1 *Generation of physically consistent profiles*

As discussed above, the process of retrieving atmospheric humidity profiles has been accelerated by the use of ANN. The atmospheric profiles required for running the LibRadtran should be physically consistent or physically based, taking care of the atmospheric dynamic processes involved. The Advanced Research WRF (ARW-WRF) (Skamarock *et al.* 2005) has been used to achieve the same. The ARW is a community numerical weather prediction model. The ARW model solves the basic four

primitive equations of fluid motion with either a hydrostatic or non-hydrostatic assumption. ARW follows $\sigma$ vertical coordinates which is commonly used in many atmospheric hydrostatic models.

$$\eta = \frac{p_h - p_{ht}}{\mu} \tag{9}$$

where

$$\mu = p_{hs} - p_{ht}. \tag{10}$$

In equation (9), $p_h$ refer to the hydrostatic component of the pressure, whereas $p_{ht}$ and $p_{hs}$ refer to the top and surface pressure of the model, respectively. The value of $\eta$ varies from 0 at the surface to 1 at top of the model pressure level. The flux form of the Euler equations are solved numerically with third-order Runge–Kutta scheme (RK3).

Table 3. *Physics paramterizations used in WRF simulations.*

| Physics | Scheme |
|---|---|
| Microphysics | Kessler scheme |
| Convective | Kain–Fritsch scheme |
| Long-wave radiation | RRTM |
| Short-wave radiation | Goddard scheme |
| Surface layer | MYJ surface scheme |

The RK3 scheme solves the governing equation for prognostic variables in three steps.

$$\Phi^* = \Phi^t + \frac{\Delta t}{3} R(\Phi^t) \tag{11}$$

$$\Phi^{**} = \Phi^t + \frac{\Delta t}{2} R(\Phi^*) \tag{12}$$

$$\Phi^{t+\Delta t} = \Phi^t + \Delta t R(\Phi^{**}) \tag{13}$$

where, $\Phi^t$ refers to the prognostic variables at time $t$ and $R(\Phi^t)$ refers to the model equations. The Courant number limitation on the model time step $\Delta t$ can be written as:

$$\Delta t_{\max} < \frac{Cr_{\text{theory}}}{\sqrt{3}} \times \frac{\delta x}{u_{\max}}. \tag{14}$$

For more details on the stability criterion, time split integration and spatial discretization, please refer to Skamarock *et al.* (2005). Arakawa C grid staggering is used in WRF. In such a staggered grid, horizontal wind components $U$ and $V$ are defined along the normal cell face whereas all other thermodynamic properties $\Theta$ are defined at the center of each grid. The initial and boundary conditions required by the pre-processor in

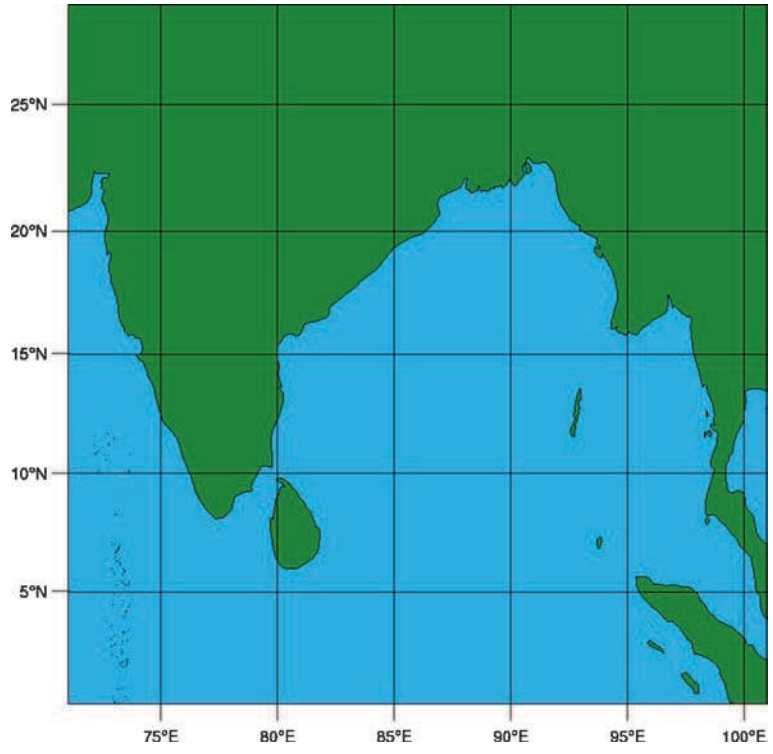


Figure 5. Domain used for running WRF.

WRF is supplied with the Global Forecast System data at a resolution of 1° × 1°, which are available every 3 hrs. The same has been downloaded from NOAA (http://nomads.ncdc.noaa.gov/data/gfs4/) and the model was initialized from $T-6$ hours, where $T$ is the time at which the INSAT 3D observations are available. To allow the model to get stabilized, initial spin-up time was taken in to account. There are a huge variety of parametrization schemes available in WRF in order to account for the sub-grid processes. Since we are focused on the clear sky scenarios, the sensitivity of the forecast to different parametrization schemes were not carried out. The parametric schemes used in this study are elaborated in table 3.

The WRF domain considered in this study is shown in figure 5. In the present study, the model resolution was taken as 6 km × 6 km with 31 $\eta$ levels, which gives a total of 32,400 pixels in each WRF run over the above domain. Since the focus of the present retrieval studies is clear sky condition, it is very important to identify and remove the cloudy pixels. As mentioned earlier, there are three window channels available in the infrared sounder of INSAT 3D. These channel radiances were used to identify the cloudy pixels by means of threshold values available in the literature. Since there is a resolution change between the sounding instrument and the WRF domain, a collocation strategy was used to identify the common pixels. The collocation is based on the minimum distance strategy which is shown in equation (15).

$$d_j = \sqrt{(\text{lat}_{\text{INSAT}} - \text{lat}_{\text{WRF}})^2 + (\text{lon}_{\text{INSAT}} - \text{lon}_{\text{WRF}})^2} \quad (15)$$

In equation (15), $j$ refers to the $j$th INSAT 3D pixel. The minimum criterion for $d$ was chosen

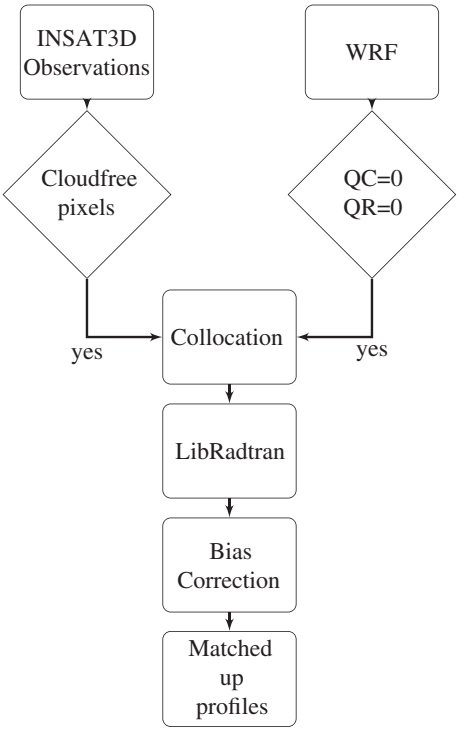


Figure 6. Generation of physically consistent profiles.

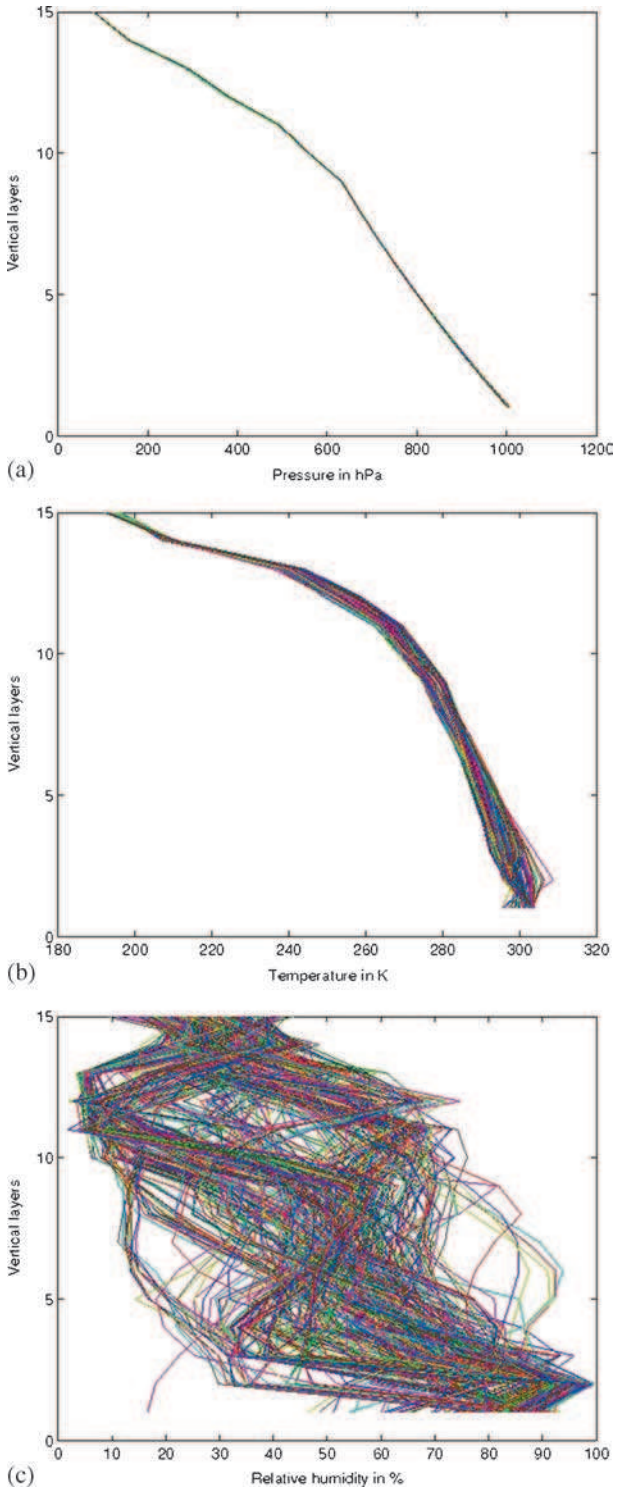


Figure 7. Generated database of (**a**) pressure, (**b**) temperature, and (**c**) humidity profiles.

to be ∼1 km. After successful collocation, the bias correction of channel-wise brightness temperatures (BTs) was carried out. The above-mentioned procedure is shown as a flow diagram in figure 6.

The generated database of geo-parameters of interest, viz., pressure, temperature and specific humidity are shown in figures 7(a, b and c). It is evident that especially the humidity data are very diverse in the whole range of relative humidity which can be seen from the eigen vector plots of the dataset, which is more representative of the spread inherent in the profiles (figure 8).

### 6.2 *Bayesian retrieval methodology*

The above-developed diverse database of humidity profiles were further used for accessing the humidity retrieval performance in a Bayesian sense. The Bayesian statistical framework has been used widely for the inverse problems in the last few decades. The formulation of the Bayesian retrieval is as follows:

$$P(\Theta|Y) = \frac{P(Y|\Theta)P(\Theta)}{P(Y)} \tag{16}$$

where $\Theta$ is the state to be estimated given the measurement vector $Y$. $P(\Theta)$ is our prior belief about the state under consideration. The priors can be information or non-informative. $P(Y|\Theta)$ is the likelihood probability in this case. It is nothing but the mapping between the parameter space and the observation space. Finally $P(\Theta|Y)$ is the posterior probability density function of $\Theta$ given $Y$. The maximum *a posteriori* (MAP) estimate can be viewed as a maximum likelihood estimate when a uniform prior $P(\Theta) \propto 1$

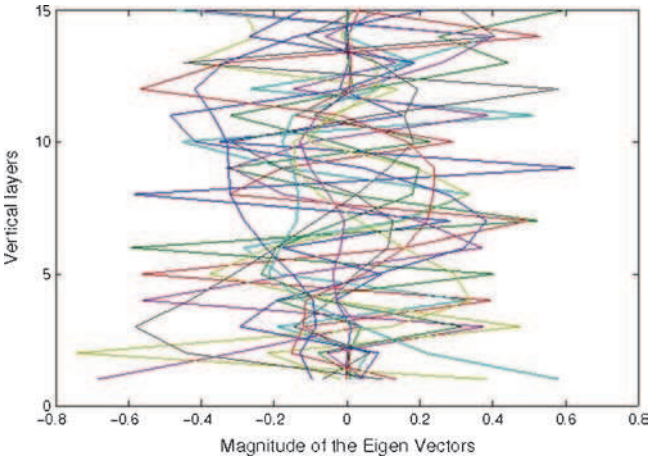


Figure 8. Eigen vectors of humidity profiles.

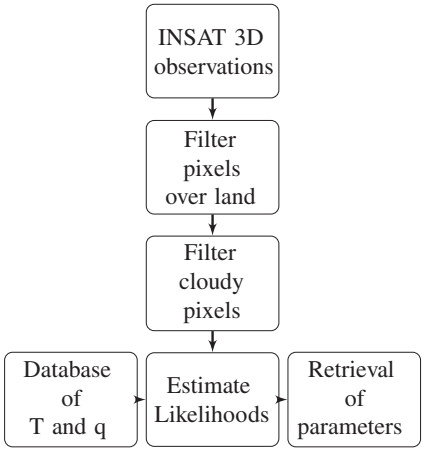


Figure 9. Overview of Bayesian retrieval.

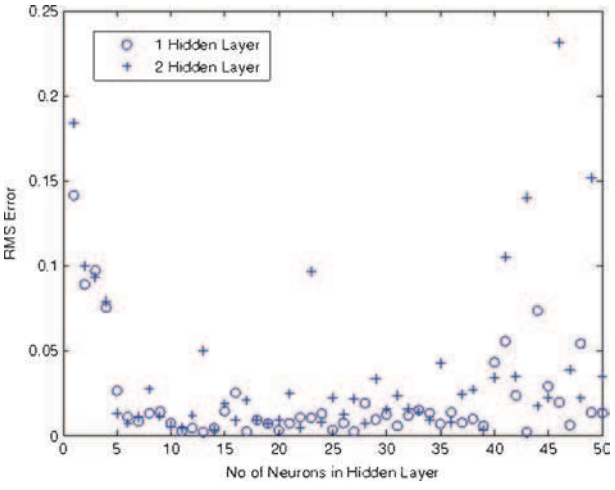


Figure 10. Variation of RMS error with the number of hidden neurons and hidden layers.

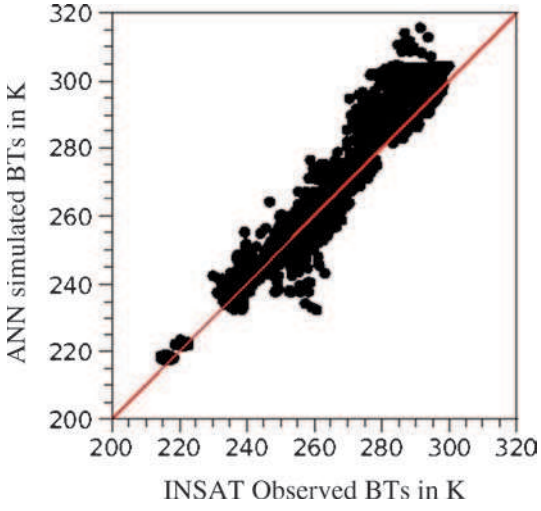


Figure 11. Partity between ANN simulated and observed BTs.

is used in equation. The normalizing constant $P(Y)$ is taken as $\int P(Y|\Theta)P(\Theta)$. For the discrete case, the integration can be replaced with a summation. From the above equation, we can calculate the expectation of a particular state as follows:

$$E(\hat{\Theta}) = \frac{\sum \Theta_j W_j}{\sum W_j} \tag{17}$$

In equation (17), the weight $W_j$ can be calculated as:

$$W_j = \frac{1}{\sqrt{2\pi}\sigma} e^{\frac{-(Y_O - Y_S)^2}{2\sigma^2}} \tag{18}$$

where $Y_O$ and $Y_S$ are observed and simulated radiances respectively and $\sigma$ is the standard deviation of the radiance data under consideration. From the above, it can be seen that the estimated state $\theta$ is nothing but a weighted estimate of all candidates from the database. Figure 9 elucidates the

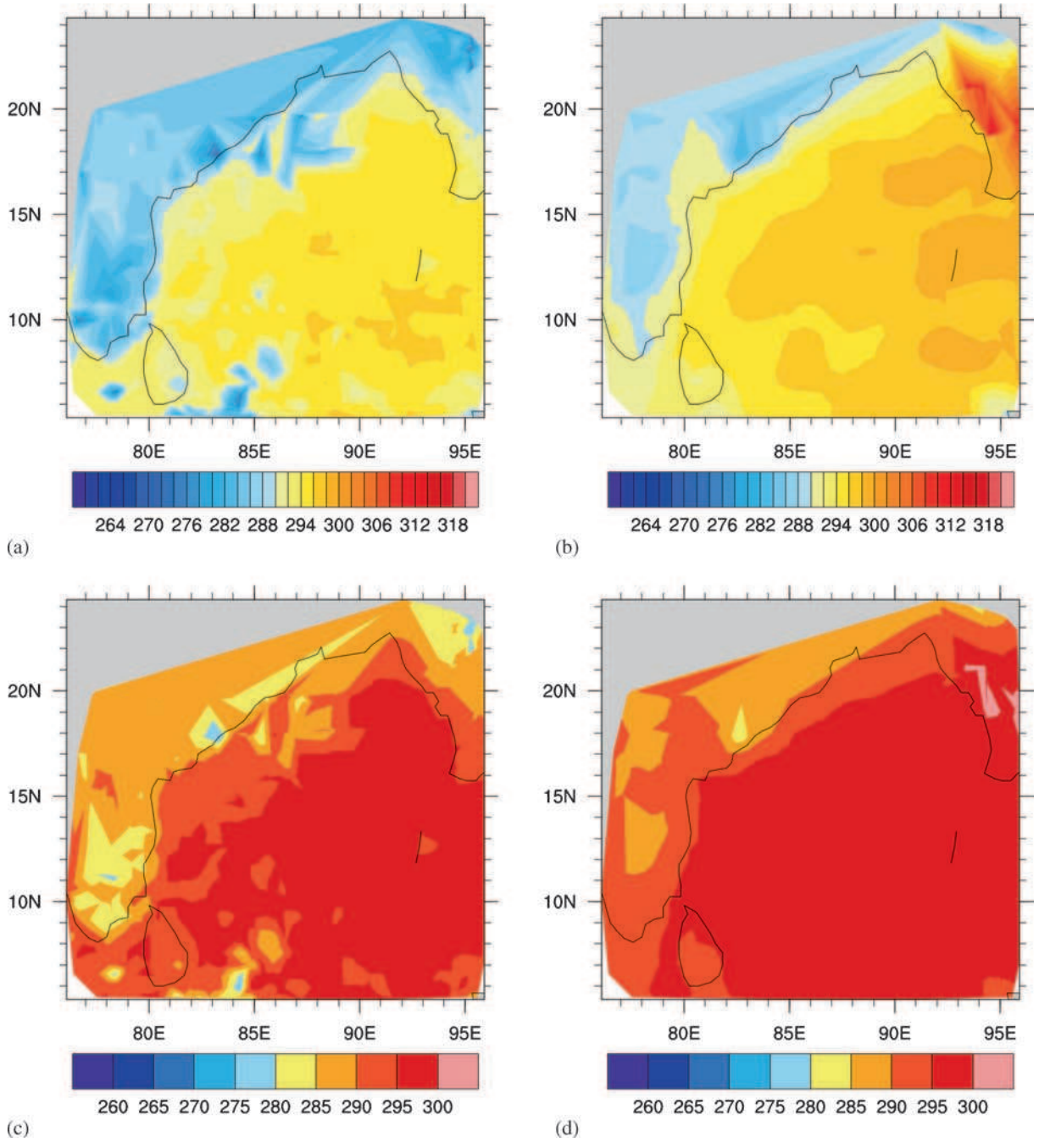


Figure 12. Comparison between observed and ANN simulated BTs for (**a** and **b**) water vapor channel and (**c** and **d**) window channel.

overall Bayesian retrieval methodology for temperature and humidity retrieval.

## 7. Results and discussion

### 7.1 *Parametric studies on the fast-forward model*

The procedure elucidated above for obtaining physically consistent profiles was carried out for different cloud free days during the months of March–September 2014, the rationale behind this wide consideration is to capture the whole range of clear sky conditions. Once the dataset was populated and bias correction of the simulated BTs done, about 80% of the data were used for training the neural network. The rest of the data were used to access the performance of the neural network, viz., root mean squared (RMS) error and so on. The parameters of paramount importance in order to select the best network candidate are number of neurons in the hidden layer, number of hidden layers and the transfer function being used. The minimization algorithm involved in arriving at the

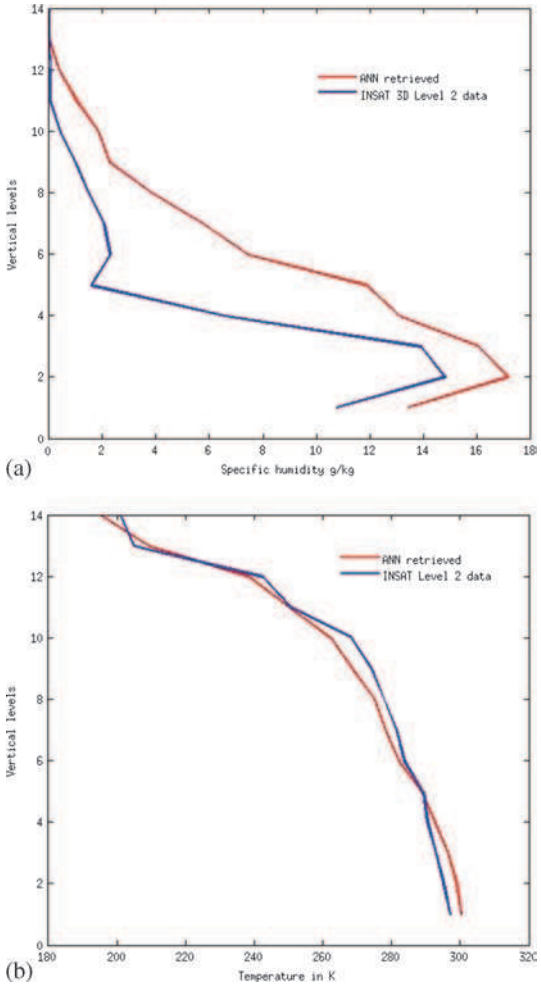


Figure 13. Comparision of (**a**) retrieved humidity profile in a humidity only retrieval experiment and (**b**) retrieved temperature profile in a temperature only retrieval experiment.

Table 4. *RMS error associated with humidity retrievals.*

| Humidity only retrieval | Combined retrieval |
|---|---|
| Min: 1.28 g/kg | Max: 1.61 g/kg |
| Max: 8.72 g/kg | Max: 9.34 g/kg |

Table 5. *RMS error associated with temperature retrievals.*

| Temperature only retrieval | Combined retrieval |
|---|---|
| Min: 1.28 K | Min: 1.61 K |
| Max: 5.72 K | Max: 5.84 K |

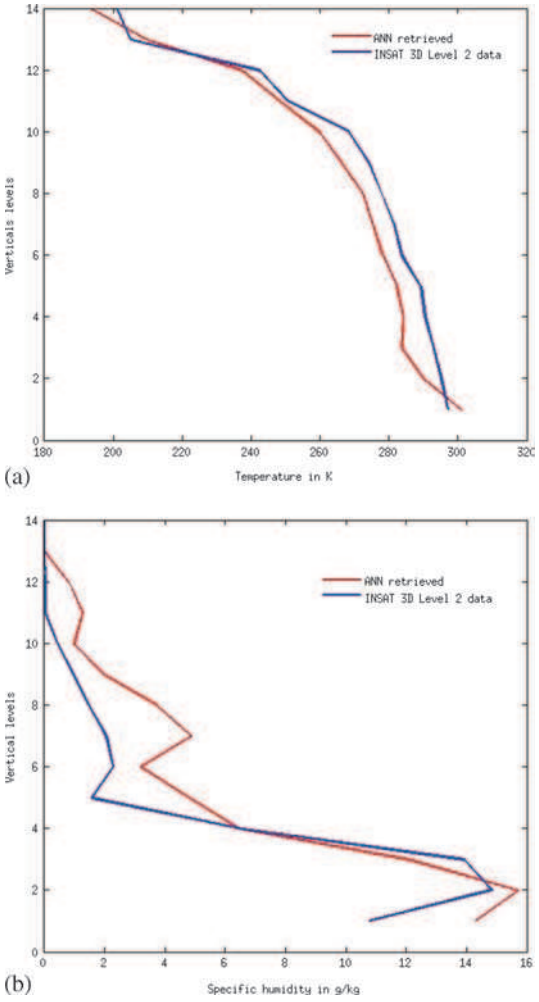


Figure 14. Comparison of retrieved (**a**) temperature and (**b**) humidity profiles in a simultaneous retrieval experiment.

optimal weight is of considerable importance. So the number of neurons in a hidden layer is varied between 1 and 50 and the number of hidden layer is kept either 1 or 2. The network performance was accessed using the RMS error calculated from the remaining data as aforementioned. Figure 10 shows the variation of the RMS error for a network with various number of hidden layers.

It can be inferred that a network with 44 neurons with 1 hidden layer performs better. Moreover, it is a well established fact that when the number input parameters far exceed the number of outputs, then the neural network will perform better. Supporting the former argument, figure 11 shows the parity plot between simulated and observed BTs from INSAT 3D. The value of correlation coefficient was found to be 0.97.

Figure 12 shows the observed and ANN simulated BTs for a water vapour channel centered around 12.02 μm and for a window channel centered around 11.03 μm. Also from the figure, it is evident that the ANN-based fast-forward model is able to predict the cloud-free scenario with much ease. Thus, it can be concluded that the ANN performs extremely well as proxy for the forward radiative transfer calculations. Furthermore, the fast-forward model developed ascertains the quality of the developed realistic database. It can be concluded that the database covers a whole range of clear sky scenarios.

### 7.2 *ANN-based geophysical retrievals*

It is evident from the above discussions that an ANN-based forward model performs well. By the same token, an ANN-based brute force retrieval was also attempted. From the above-developed database of geophysical parameters, viz., pressure, temperature and relative humidity, three different classes of retrievals were performed in order to arrive at the best retrieval strategy, viz., (1) temperature only retrieval, (2) humidity only retrieval, and (3) simultaneous retrieval of temperature and humidity.

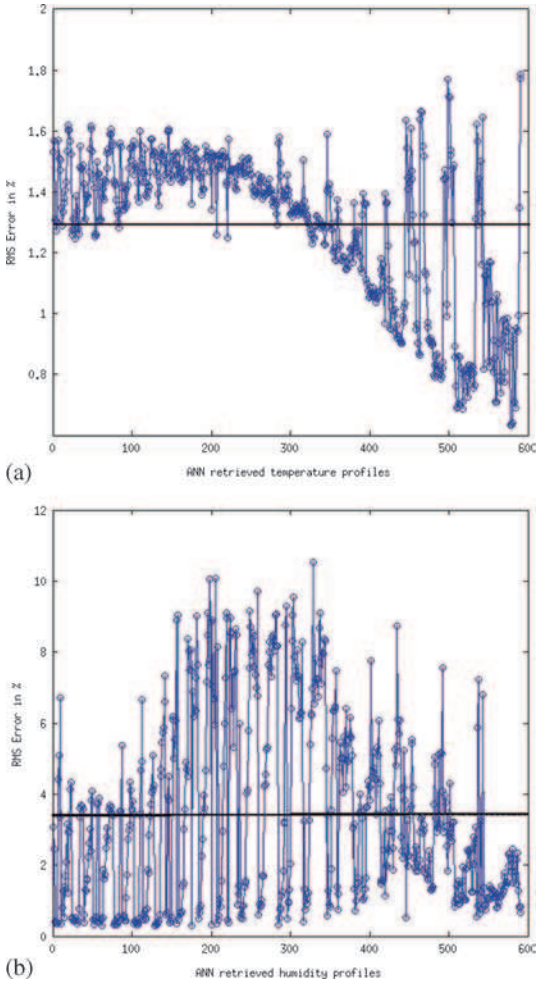


Figure 15. RMS error in a sample (**a**) humidity and (**b**) temperature ANN retrieval.

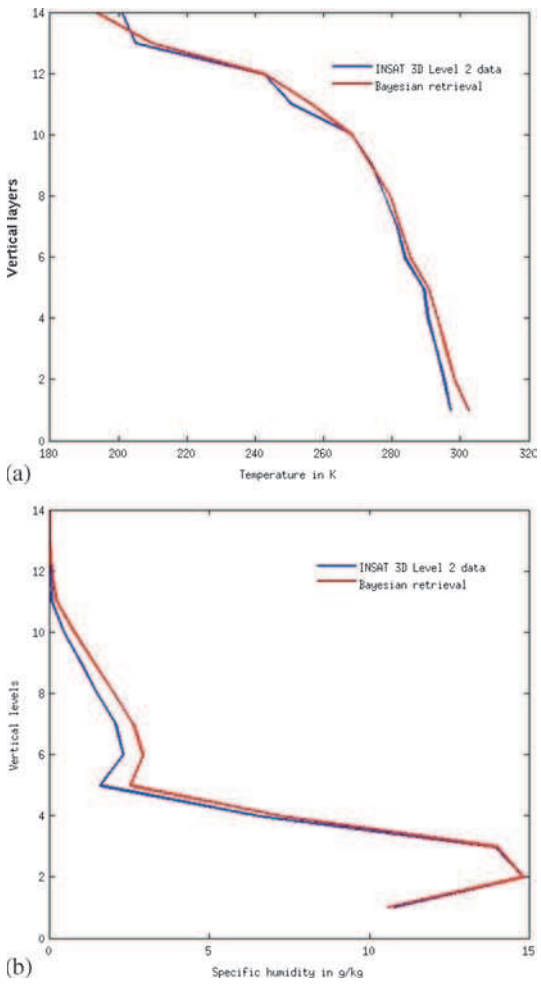


Figure 16. Comparison of retrieved (**a**) temperature and (**b**) humidity profiles in a Bayesian retrieval experiment.

### 7.2.1 *Temperature and humidity only retrieval*

An ANN was trained with the 18 channel simulated BTs as input with the 15 layer temperature/humidity as output. The above-mentioned parametric studies were carried out to arrive at the best neural network architecture. Once we have decided upon the best neural network architecture, actual INSAT 3D observed BTs were used to retrieve the humidity profiles. Since we have used the clear-sky conditions as the input and their corresponding radiance response as the output, we need to filter the cloudy pixels from the measurement data again. First, the clear sky pixels were identified. Since the above database was constructed by gathering thermodynamic profiles over the ocean, it is inevitable to filter out the pixels over the land. After successful collocation, the retrievals were performed. Figure 13(a) shows a comparison of a sample retrieved humidity profile for cloud-free condition with the INSAT 3D Level 2 data from MOSDAC (www.mosdac.gov.in). The RMS error associated with the humidity only retrieval is shown in table 4. The layerwise RMS error of all shows a maximum error of 8.72 g/kg near the surface.

Figure 13(b) shows the comparison for the temperature retrieval. From table 5, the maximum RMS error associated with the ANN only temperature retrieval is 5.722 K.

### 7.2.2 *Simultaneous temperature and humidity retrieval*

The third case of simultaneous retrieval was accomplished by training the network with the 18 channel BTs as input and layerwise values of both temperature and humidity as output. As aforementioned, after zeroing on the best network architecture, retrieval experiments were performed with the actual INSAT 3D observations. Figure 14(a) shows a comparison of the retrieved temperature and Level 2 data. Similarly, the humidity counterpart is shown in figure 14(b). The RMS errors for

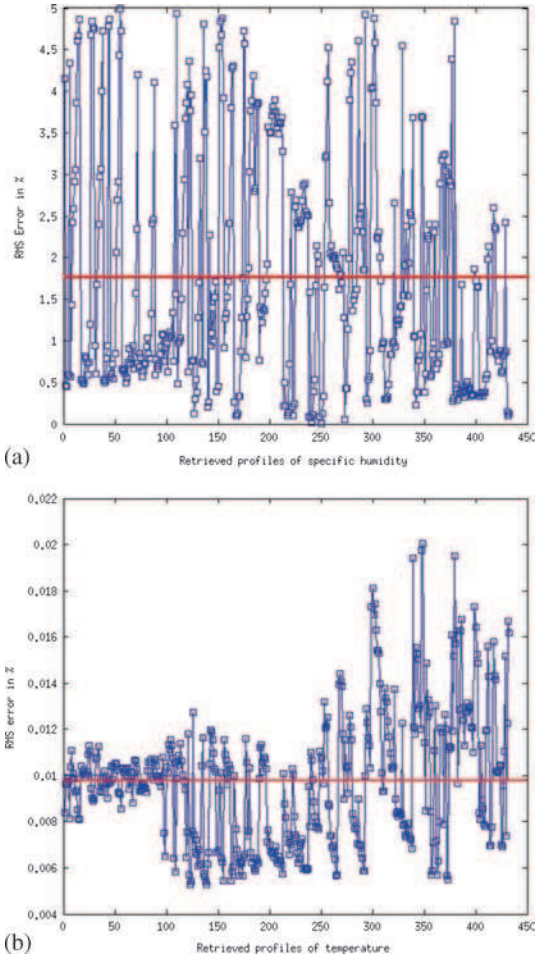


Figure 17. RMS error in a sample (**a**) humidity and (**b**) temperature Bayesian retrieval.

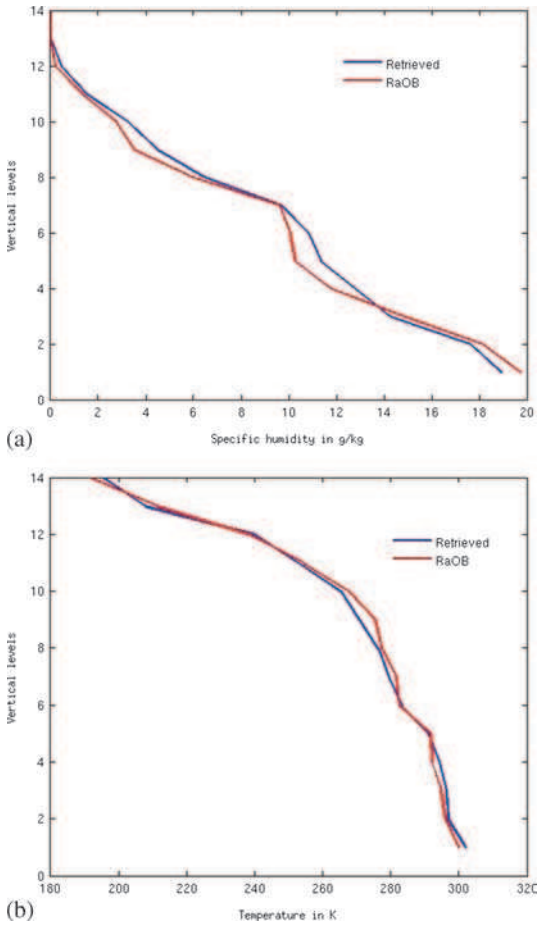


Figure 18. Comparison of retrieved (**a**) temperature and (**b**) humidity profile with RaOB for station: 23459.

the simultaneous retrieval of humidity and temperature can be seen in tables 4 and 5. It can be seen that the maximum error incurred in the humidity and temperature retrieval are 9.343 g/kg and 5.843 K, respectively. Eventhough the ANN architecture is not a compression type of network, the errors associated with the combined retrieval increases only marginally when compared with humidity and temperature alone retrievals. Also shown in figure 15(a and b) is the RMS error variation for the sample retrieved profiles of temperature and humidity. The average RMS error in the retrieval was found to be 1.29% for temperature and 3.4% for humidity.

### 7.3 *Bayesian retrieval of temperature and humidity*

The above described Bayesian likelihood estimation is used as a retrieval tool for retrieving simultaneously temperature and humidity from 18 channel BTs measured by INSAT 3D. The $\sigma$ was calculated from the covariance matrix of the BTs from the database. The INSAT 3D measurements for a clear sky scenario were taken and the retrievals were performed. Figure 16(a and b) shows a comparison of the retrieved temperature and humidity profiles with the INSAT 3D Level 2 derived data.

The RMS error associated with the retrieval is shown in figure 17(a and b) for humidity and temperature respectively. The average RMS error in retrieved humidity profile was found to be 1.7%, whereas for the temperature it was observed to be 0.01%. When compared with simultaneous retrieval using an ANN, Bayesian retrieval methodology proves highly superior since the ANN architecture used for simultaneous retrieval was not a compression type of network. The errors in the retrieved humidity and temperature profiles can be minimized when suitable priors for temperature and humidity are used.

The Bayesian retrieval framework was compared with *in-situ* radiosonde observations extracted from NCEP ADP Upper Air Data by collocating the coordinates of observations over ocean with INSAT 3D pixels and three different locations with station ids 23459, 23009 and 23094 were used for comparison. The corresponding latitude

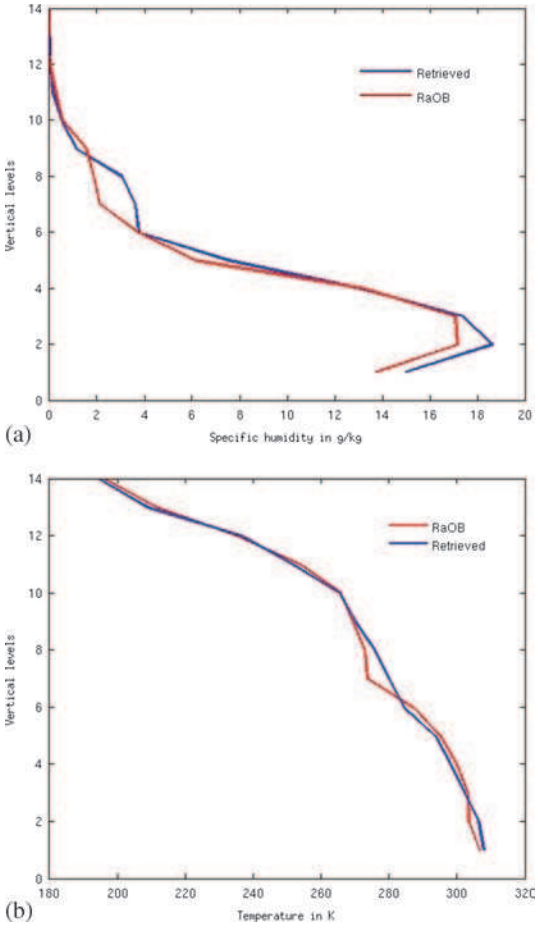


Figure 19. Comparison of retrieved (**a**) temperature and (**b**) humidity profile with RaOB for station: 23009.

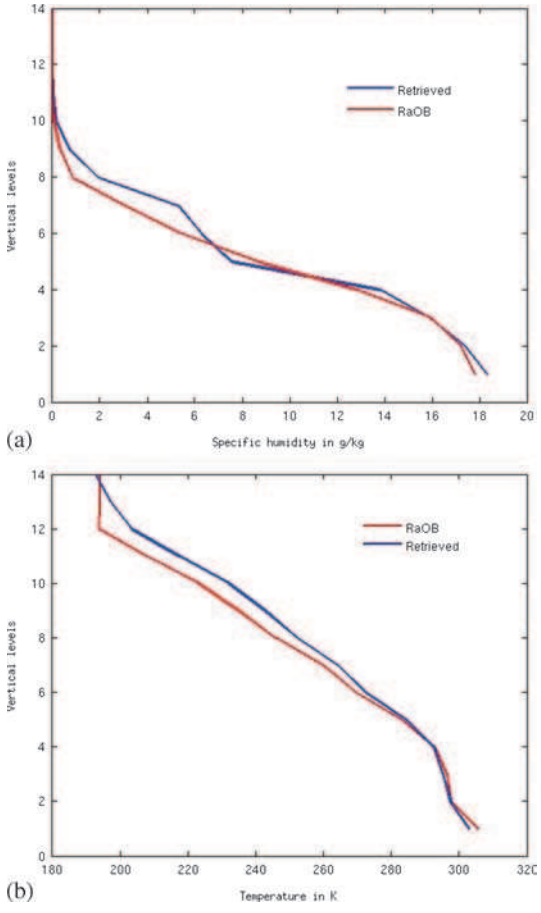


Figure 20. Comparison of retrieved (**a**) temperature and (**b**) humidity profile with RaOB for station: 23094.

and longitude coordinates are $(14.01°, 87.0°)$, $(15.0°, 89.96°)$ and $(13.48°, 83.98°)$ repectively. The agreement between the retrieved profiles of temperature and humidity can be seen in figures 18(a)–20(b). The comparison shows an RMS error of 3.52 g/kg in humidity and 3.78 K in temperature.

## 8. Conclusions

The present work reports the development of an ANN-based fast-forward model as a proxy for the existing line-by-line solvers for simulating the upwelling radiances associated with the channels present in infra-red sounder aboard INSAT 3D. A diverse set of physically consistent profiles of $P$, $T$ and $q$ was arrived at by using a dynamic weather model WRF. The fast forward model was trained and experimented with the realistic database and a good correlation was observed when compared with the observed BTs. Thus the exhaustiveness of the developed database of geo-parameters were ascertained. Two retrieval techniques, namely, (1) an ANN-based retrieval and (2) Bayesian likelihood retrieval were performed using the observed radiances from INSAT 3D infrared sounder. In the ANN-based retrieval itself three different configurations were numerically experimented. A comparison of the two retrieval techniques were made for a clear sky scenario observed by the INSAT 3D instrument and the resulting RMS errors observed in different techniques were also highlighted. Comparison of the retrieved results with the radiosonde observations was also done. In view of the above results, it can be concluded that the diverse set of profiles developed were more representative of most of the clear sky scenarios. By a careful scrutiny of the outcomes it can be concluded that:

1. The realistic database has a diverse nature with respect to humidity and temperature.
2. The comparison made with humidity/temperature only retrievals, showed better results compared to the combined retrieval of temperature and humidity.
3. The simultaneous retrieval of temperature and humidity using Bayesian technique outperforms ANN in terms of the RMS error.

The developed database not only filters the pixels over land, but also the pixels which are deemed to be cloudy and this poses as a limitation of the retrieval methodology developed. Eventhough there is an exhaustiveness inherent in the developed database, the retrieval performance can be even improved by assuming an *a-priori* for the parameters and this is underway.

## References


Ajil K S, Thapliyal P K, Shukla M V, Pal P K, Joshi P C and Navalgund R R 2010 A new technique for temperature and humidity profile retrieval from infrared-sounder observations using the adaptive neuro-fuzzy inference system; *Geosci. Remote Sens., IEEE Trans.* **48(4)** 1650–1659.

Balaji C and Ramanujam K S 2013 Retrieval of the vertical rainfall structure from the MADRAS imager data of the Megha-Tropiques satellite; *Curr. Sci.* **104(12)** 16–27.

Cabrera-Mercader C and Staelin D 1994 Passive microwave humidity profile retrievals using neural networks; In: Geoscience and Remote Sensing Symposium, IGARSS'94. Surface and Atmospheric Remote Sensing: Technologies, Data Analysis and Interpretation, *IEEE* **4** 2057–2059.

Churnside J H, Stermitz T A and Schroeder J A 1994 Temperature profiling with neural network inversion of microwave radiometer data; *J. Atmos. Oceanic Technol.* **11(1)** 105–109.

Hewison T J 2007 1D-var retrieval of temperature and humidity profiles from a ground-based microwave radiometer; *Geosci. Remote Sens., IEEE Trans.* **45(7)** 2163–2168.

Jieying H, Shengwei Z, Yingzhu H, Yu Z and Fenglin S 2010 The humidity retrievals using BP neural network algorithm based on mexihat or morlet wavelet function in clear-sky; In: *Antennas Propagation and EM Theory* (*ISAPE*), 9th International Symposium, *IEEE*, pp. 502–504.

Jones C, Peterson P and Gautier C 1999 A new method for deriving ocean surface specific humidity and air temperature: An artificial neural network approach; *J. Appl. Meteorol.* **38(8)** 1229–1245.

Katti V, Pratap V, Dave R and Mankad K 2006 INSAT-3D: An advanced meteorological mission over Indian Ocean; International Society for Optics and Photonics.

Krishnan P, Ramanujam K S and Balaji C 2012 An artificial neural network based fast radiative transfer model for simulating infrared sounder radiances; *J. Earth Syst. Sci.* **121(4)** 891–901.

Marécal V and Mahfouf J-F 2000 Variational retrieval of temperature and humidity profiles from TRMM precipitation data; *Mon. Weather Rev.* **128(11)** 3853–3866.

Marzano F S, Botta G and Montopoli M 2010 Iterative Bayesian retrieval of hydrometeor content from x-band polarimetric weather radar; *Geosci. Remote Sens., IEEE Trans.* **48(8)** 3059–3074.

Mayer B and Kylling A 2005 Technical note: The libRadtran software package for radiative transfer calculations – description and examples of use; *Atmos. Chem. Phys.* **5(7)** 1855–1877.

McFarlane S A, Evans K F and Ackerman A S 2002 A Bayesian algorithm for the retrieval of liquid water cloud properties from microwave radiometer and millimeter radar data; *J. Geophys. Res. Atmos.* **107(D16)** AAC–12.

Phalippou L 1996 Variational retrieval of humidity profile, wind speed and cloud liquid-water path with the SSM/I: Potential for numerical weather prediction; *Quart. J. Roy. Meteorol. Soc.* **122(530)** 327–355.

Ramanujam S, Chandrasekar R and Chakravarthy B 2011 A new pca-ann algorithm for retrieval of rainfall structure in a precipitating atmosphere; *Int. J. Numerical Methods for Heat & Fluid Flow* **21(8)** 1002–1025.

Rothman L S, Jacquemart D, Barbe A, Benner D C, Birk M, Brown L, Carleer M, Chackerian C, Chance K and Coudert L H *et al*. 2005 The HITRAN 2004 molecular spectroscopic database; *J. Quant. Spectrosc. Rad. Transfer* **96(2)** 139–204.

Shi L 2001 Retrieval of atmospheric temperature profiles from amsu – a measurement using a neural network approach; *J. Atmos. Oceanic Technol.* **18(3)** 340–347.

Skamarock W C, Klemp J B, Dudhia J, Gill D O, Barker D M, Wang W and Powers J G 2005 A description of the advanced research WRF version 2.

Thapliyal P, Shukla M, Bisht J, Pal P and Navalgund R 2014 Improvement in the retrieval of humidity profiles using hybrid regression technique from infrared sounder data: A simulation study; *Meteorol. Appl.* **21(2)** 301–308.

*MS received 12 May 2015; revised 13 November 2015; accepted 17 November 2015*